JNPS 10 (2): 127 – 137 (2024)
ISSN: 2392-473X (Print), 2738-9537 (Online)

Research Article ©*Nepal Physical Society*
doi.org/10.3126/jnphyssoc.v10i2.79501

Synthesis and Characterization of Fe@Cu Bimetallic Nanoparticle: Microemulsion Method

Pankaj Singh Dhami,[1] Sudeep Lamichhane,[1] Narayan Adhikari,[1,*)] and Rameshwar Adhikari[2]

[1)]*Central Department of Physics, Tribhuvan University, Kathmandu, Nepal*
[2)]*Research Center for Applied Science and Technology, Tribhuvan University, Kathmandu, Nepal*

Abstract. The primary objective of this study is to synthesize Fe@Cu bimetallic nanoparticles (BNP's) using the microemulsion technique. Microemulsion techniques are widely employed for the controlled fabrication of nanoparticles with specific shapes and dimensions. The synthesized nanoparticles were characterized using UV-Vis spectroscopy, Fourier Transform Infrared spectroscopy (FT-IR), and X-ray diffraction (XRD). X-ray diffraction analysis revealed that the crystallite sizes of the Fe@Cu bimetallic nanoparticles fell within the range of 14.52 nm. The XRD graph also indicated the presence of copper peaks at (2θ) values of 34.52°, 42.60°, 50.60°, and 74.10°, as well as an iron peak at 43.70°. Additionally, we observed several oxide peaks for both copper and iron particles at 24.50°, 29.20°, 30.00°, 31.40°, 33.10°, 37.00°, and 61.80°, suggesting that a minor portion of copper had undergone oxidation and transformed into copper oxide. Peaks at 65.10°and 83.00°indicated the presence of iron oxide. UV-Vis spectroscopy of the Fe@Cu bimetallic nanoparticles exhibited a maximum peak at (312 ± 8.20) nm, with direct and indirect band gap energies of (2.54 ± 0.20) eV and (0.26 ± 0.02) eV, respectively. Both the indirect and direct band gaps demonstrated semiconductor behavior. Furthermore, UV-Vis spectroscopy revealed the surface plasmon resonance of Cu nanoparticles at (459 ± 1.13) nm. Fourier transform infrared spectroscopy of Fe@Cu bimetallic nanoparticles identified peaks at 680.87 cm^{-1} and 607.57 cm^{-1}, confirming the presence of Cu-O bonds, which align with Fe in the core and Cu on the shell. Moreover, this study included the preparation of Cu@Fe bimetallic nanoparticles, as well as monometallic copper (Cu) and iron (Fe) nanoparticles. The characterization of these materials involved UV-Vis spectroscopy and FT-IR spectroscopy.

Submitted: November 2, 2024; **Revised**: May 30, 2024; **Accepted**: June 1, 2025

Keywords: Asymmetry; Microemulsion; Miller Indices; Nanoparticles

INTRODUCTION

Approximately 13.8 billion years ago, the Big Bang led to the formation of all the matter and energy in the universe [1, 2]. Nanoparticles and nanostructured materials are thought to have originated from the Big Bang process, when atoms and molecules condensed in the early universe. These materials have been found in meteorites, which are thought to have formed from the debris of early stars [3]. The prefix "nano-" originates from the Greek word "nanos," which means "dwarf." It refers to things that are one billionth of a meter in size [4]. The International Organization for Standardization (IOS) defines a nanoparticle as a particle with a diameter of 1 to 100 nanometers [5]. This means that nanoparticles are incredibly small, even smaller than bacteria, and nanoparticles can be found in both natural and man-made materials. Nanoparticles have a wide range of potential applications in medicine, energy, environmental remediation, materials science, manufacturing, and consumer products [6]. The term "nanotechnology" was first used by Norio Taniguchi in 1981, but the idea of working with atoms and molecules was first thought of by Richard Feynman in 1959 [7].

Microemulsion

Microemulsions exhibit both thermodynamic stability and kinetic instability They are thermodynamically stable because, when a microemulsion forms, it represents a state of lower Gibbs free energy, indicating a lower-energy state compared to the initial, unmixed state of oil and water. The presence of surfactants in microemulsions

*)Corresponding author: narayan.adhikari@cdp.tu.edu.np

plays a crucial role by reducing the interfacial tension between oil and water, thus lowering the free energy associated with the interface and contributing to the overall stability of the system This thermodynamic stability is vital, as without it, microemulsions would tend to phase separate over time. However, microemulsions are kinetically unstable because they require continuous energy input to maintain their small droplet size and prevent coalescence [8].

Microemulsions are transparent, isotropic dispersions of two immiscible liquids, such as water and oil, stabilized by surfactant molecules at the water/oil interface. The surfactant and co-surfactant molecules form a monolayer at the water/oil interface. Microemulsions are composed of water, oil, surfactant, and co-surfactant [9]. These components are mixed in carefully controlled proportions to form the microemulsion. The size of microemulsion particles ranges from about 10 to 100 nanometers (nm). This means that they are too small to be seen with the naked eye [10].

During the formation of a microemulsion, there is typically a negative change in Gibbs free energy (ΔG). This negative ΔG signifies that the process is thermodynamically stable and that the resulting microemulsion represents a lower-energy state compared to the unmixed components. This negativity of ΔG is a fundamental characteristic of microemulsion behavior and is integral to their stability [8]. Microemulsions can be classified into three different types based on their compositions and structural characteristics. In oil-in-water microemulsion, the droplet of oil phase is dispersed in water phase. These microemulsions usually contain a higher fraction of water, a lower fraction of oil, and appropriate surfactant and cosurfactant concentrations. O/W microemulsions are commonly used for drug delivery, pharmaceutical formulations, and in the food and cosmetic industries [11]. In the water-in-oil microemulsion, the droplet of water phase is dispersed in oil phase. These microemulsions usually contain a higher fraction of oil, a lower fraction of water, and appropriate surfactant and co-surfactant concentrations. W/O microemulsions are often used in the formulation of cosmetic and personal care products [12]. However, bicontinuous microemulsions have both oil and water droplets dispersed in a continuous phase of surfactant and cosurfactant [13].

PREPARATION OF SOLUTION

Preparation of Microemulsions (ME) for BNP's

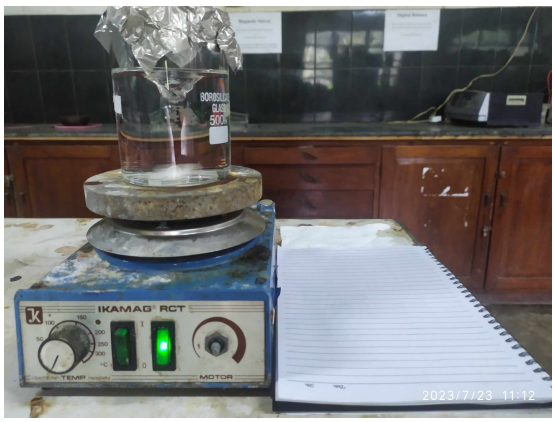

FIGURE 1: Preparation of Transparent microemulsion solution

FIGURE 2: Preparation of a microemulsion solution containing $FeSO_4 \cdot 7H_2O$.

In this work, we prepared a water-in-oil microemulsion, where a water phase is dispersed in an oil phase. To create the microemulsion, we combined 138 ml of hexane as the oil phase with 7.8 ml of distilled water, 2.4 grams of sodium lauryl sulfate as a surfactant, and 40.2 ml of iso-amyl alcohol as a co-surfactant in a 250 ml conical flask. The mixture was then placed on a magnetic stirrer and stirred for 30 minutes, then a clear and transparent 186 ml of microemulsion solution was obtained.

Figure 2 illustrates the preparation of a microemulsion solution containing $FeSO_4 \cdot 7H_2O$. This solution is prepared by utilizing one-third of the solution described in

FIGURE 3: Preparation of a microemulsion solution containing $CuSO_4 \cdot 5H_2O$.

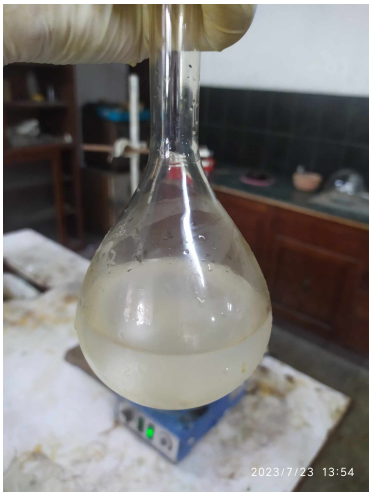

FIGURE 4: Preparation of a microemulsion solution containing $NaBH_4$.

Figure 1. To create this solution, a magnetic stirrer is employed. The magnetic stirrer generates a magnetic field, which serves as the energy source in this process. We then use the magnetic stirrer to mix $FeSO_4 \cdot 7H_2O$ for 30 minutes, resulting in $FeSO_4 \cdot 7H_2O$ being transformed into a soluble form within the solution.

Figure 3 shows the preparation of a microemulsion solution containing $CuSO_4 \cdot 5H_2O$. To prepare this solution, one-third of the solution from Figure 1 is used. A magnetic stirrer is used to mix the solution, which generates a magnetic field that serves as the source of energy. The magnetic stirrer is run for 30 minutes to dissolve the $CuSO_4 \cdot 5H_2O$.

Moving on to Figure 4, it illustrates the preparation of a microemulsion solution containing sodium borohydride ($NaBH_4$). To create this solution, one-third of the solution described in Figure 1 is utilized. In this process, a magnetic stirrer is not employed. Instead, an ice bath is utilized for the dissolution of $NaBH_4$. This decision is driven by the fact that sodium borohydride is a highly potent reducing agent. The dissolution of $NaBH_4$ in water is an exothermic process, meaning it generates heat. The use of an ice bath serves the purpose of rapidly dissipating this heat, effectively preventing the solution from becoming excessively hot. An ice bath offers a controlled and secure environment for this dissolution process.

Preparation of Fe@Cu BNP's from Microemulsion (ME) Solution

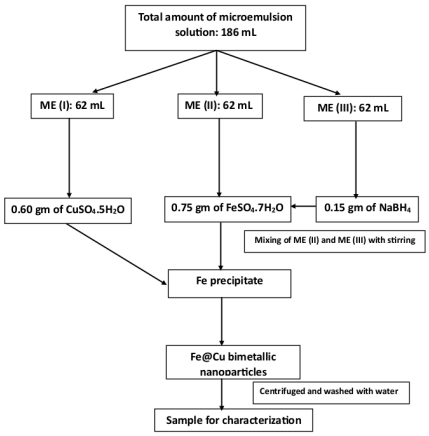

FIGURE 5: Procedure for the synthesis of Fe@Cu BNP's.

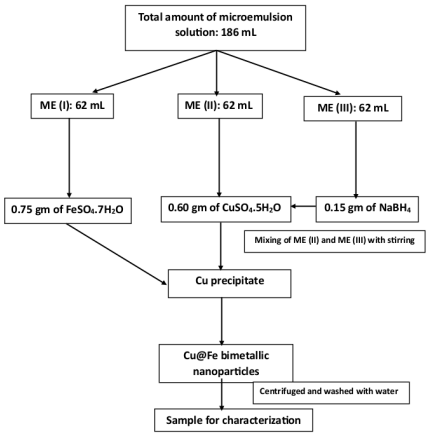

FIGURE 6: Procedure for the synthesis of Cu@Fe BNP's.

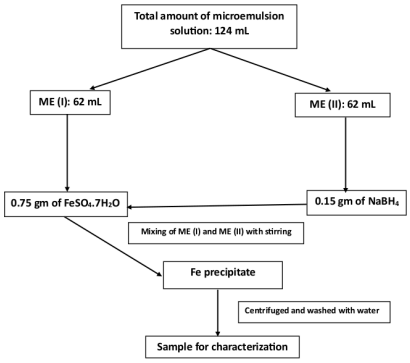

FIGURE 7: Procedure for the synthesis of Iron (Fe) MNP's.

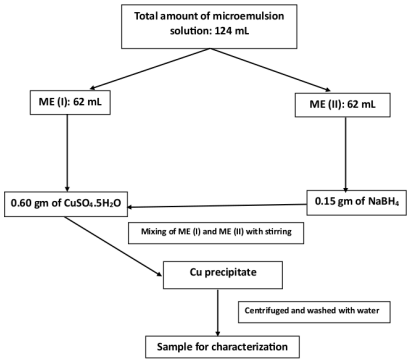

FIGURE 8: Procedure for the synthesis of Copper (Cu) MNP's.

The total microemulsion solution of 186 mL was divided into three equal parts: ME (I) contained 62 mL, ME (II) contained 62 mL, and ME (III) also contained 62 mL of microemulsion solution. In ME (I), we added 0.75 grams of the compound form of $FeSO_4 \cdot 7H_2O$, which was dissolved by stirring on the magnetic stirrer for 30 minutes. The resulting solution, representing the liquid form of $FeSO_4 \cdot 7H_2O$. In ME (II), we added 0.6 grams of the compound form of $CuSO_4 \cdot 5H_2O$, which was also dissolved by stirring on the magnetic stirrer for 30 minutes. The resulting solution, representing the liquid form of $CuSO_4 \cdot 5H_2O$. Another microemulsion (III) was prepared by dissolving 0.15 grams of $NaBH_4$, in an ice bath without using a magnetic stirrer. Then, the $NaBH_4$ microemulsion solution and the $FeSO_4 \cdot 7H_2O$ microemulsion solution were gradually mixed with constant stirring using a burette while maintaining constant stirring. This mixing process led to the formation of a precipitate in the form of iron (Fe) nanoparticles. Finally, the remaining $CuSO_4 \cdot 5H_2O$ microemulsion solution was added dropwise using a burette to obtain an iron-precipitated solution. A reddish brown bimetallic nanoparticle (BNP's) appeared, signifying the formation of Fe@Cu bimetallic nanoparticles (BNP's). The prepared bimetallic nanoparticles (BNP's) were washed several times in a centrifuge and dried in a convection oven at 40 °C for 1 hour. Finally, the dried samples were transferred to sealed vials for further use.

The flowchart for the synthesis of Fe@Cu bimetallic nanoparticles using microemulsion is shown in Figure 5. Additionally, in our research, we also prepared Cu@Fe bimetallic nanoparticles, as well as iron (Fe) and copper (Cu) monometallic nanoparticles. The preparation processes for these nanoparticles are depicted in the given flowcharts.

RESULTS AND DISCUSSION

UV-Vis Absorption Analysis of Fe@Cu, Cu@Fe, Copper (Cu), and Iron (Fe) Nanoparticles

UV-Visible spectroscopy is based on the principle of electronic transitions, where the absorption of UV-Visible light by electrons provides information about the electronic structure and concentration of absorbing species in a sample. In this section, we have plotted UV-Visible graphs for bimetallic Fe@Cu and Cu@Fe nanoparticles as well as monometallic copper (Cu) and iron (Fe) nanoparticles.

The UV-Vis absorption data of the synthesized Fe@Cu bimetallic nanoparticles, with iron (Fe) in the core and copper (Cu) on the shell, reveal that UV light directly interacts with the copper nanoparticles. As anticipated, the absorbance peak of copper nanoparticles broadly increases starting from the 539 nm region, attributable to the surface plasmon resonance (SPR) of copper nanoparticles. Additionally, a band centered at 345 nm aligns with reference values for the absorption band of Cu nanoparticles [14, 15]. The absorbance value exceeds 1.5 due to high sample concentration; dilution during UV exposure would decrease the absorbance peak to less than one, an ideal scenario.

In the synthesis of Cu@Fe bimetallic nanoparticles, where copper (Cu) forms the core and iron (Fe) the outer shell, UV light directly interacts with the iron (Fe) nanoparticles. Interestingly, no broad peak formation is observed in the copper-associated region, indicating exclusive interaction of the light source with iron particles. Furthermore, the absorbance values for iron exhibit a significant shift by 280 nm, still falling within the established 280–350 nm range for iron nanoparticle absorption. Notably, no discernible sharp absorption bands are observed within the copper absorption range. These observations strongly suggest the formation of iron particles in the shell, with

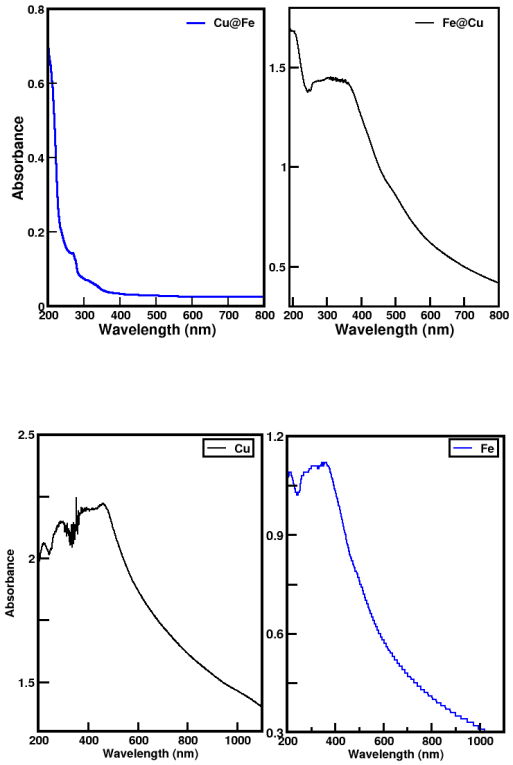

FIGURE 9: UV-Vis analysis of bimetallic (up) and monometallic (down) nanoparticles.

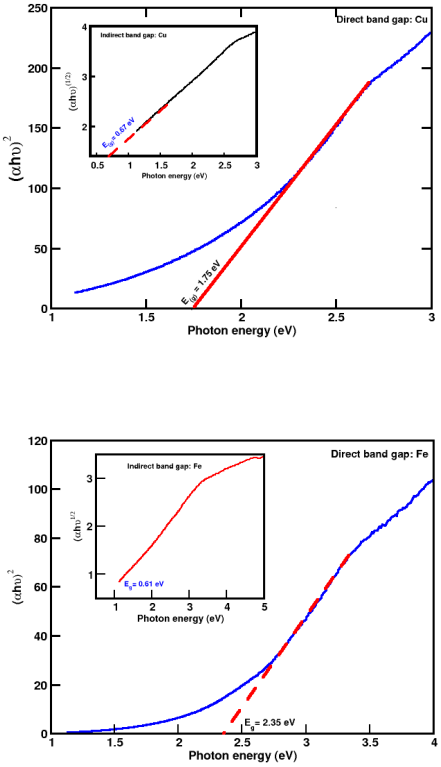

FIGURE 10: Direct and indirect band gaps of Copper (up) and Iron (down) monometallic nanoparticles.

copper predominantly in the core. The absence of sharp absorption bands in the copper range further supports this conclusion. Generally, an absorbance value below 0.8 indicates high sample concentration and significant light absorption [14]. The broad absorption peak of copper nanoparticles, located at (459 ± 1.13) nm, is attributed to the surface plasmon phenomenon [16, 17]. The UV spectrum of iron nanoparticles exhibits a peak at (340 ± 9.60) nm. Notably, dilution of the sample will result in a decrease in high absorbance.

Tauc plot Analysis of Copper (Cu) and Iron (Fe) MNP's

The optical band gap (E_g) of a nanomaterial can be determined using the Tauc and Davis-Mott relation [18, 19], which establishes a connection between the optical absorption coefficient (α) and the band gap energy (E_g). The relation is expressed as: $(\alpha h\nu)^2 = A(h\nu - E_g)$ Where (ν) is the photon's frequency, h is Planck's constant, α is the absorption coefficient, A is a constant, and E_g is the band gap energy [20].

The direct and indirect band gap energies of copper monometallic nanoparticles are approximately (1.75 ± 0.06) eV and (0.67 ± 0.01) eV, respectively. These band gap values suggest that the sample likely behaves as a semiconductor, which can be attributed to the presence of oxygen (oxidation). When metals undergo oxidation, they typically transition from being conductors to semiconductors or insulators [21, 22]. Similarly, for iron monometallic nanoparticles, the direct and indirect band gap energies are approximately (2.35 ± 0.24) eV and (0.61 ± 0.06) eV, respectively. These values indicate that iron nanoparticles also exhibit semiconductor behavior, similar to that of a wide-range semiconductor [23].

Tauc plot Analysis of Fe@Cu and Cu@Fe BNP's

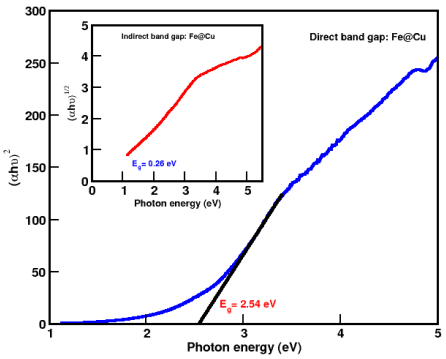

FIGURE 11: Direct and indirect band gaps of Fe@Cu bimetallic nanoparticles.

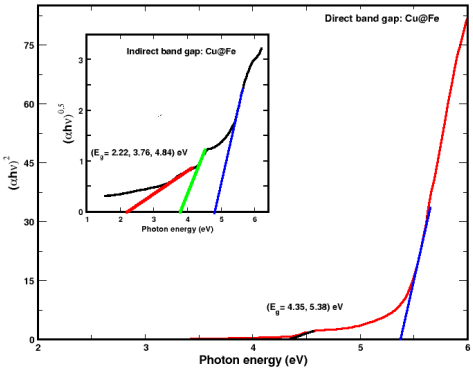

FIGURE 12: Direct and indirect band gaps of Cu@Fe bimetallic nanoparticles.

The Tauc plot analysis of Fe@Cu bimetallic nanoparticles, with band gap energies of (2.54 $\pm$ 0.29) eV and (0.26 $\pm$ 0.02) eV, suggests that the material exhibits characteristics of both insulators and semiconductors. These band gaps (2.54 $\pm$ 0.29) eV and (0.26 $\pm$ 0.02) eV are indicative of p-type semiconductor properties [24]. In the case of Cu@Fe bimetallic nanoparticles (BNP's), the direct and indirect band gaps measured (2.22, 3.76, 4.84) eV and (4.35 $\pm$ 0.30, 5.38 $\pm$ 0.30) eV, respectively. These band gap values suggest that the sample exhibits wide-range semiconductor behavior. This behavior can be attributed to the presence of oxygen in the sample, causing it to take on an oxide form and exhibit such characteristics. If the sample were created in an inert atmosphere, it would likely reduce the band gap range, transforming it into either a conductor or a pure semiconductor [25].

FT-IR SPECTROSCOPY ANALYSIS OF COPPER (CU) AND IRON (FE) MNP'S

The peak at 601.79 cm^{-1} indicates the presence of Cu monometallic nanoparticles. According to the literature, the main absorption stretch for copper nanoparticles is typically found between 615 and 619 cm^{-1} [26]. Additionally, other studies have reported strong absorption bands for Cu-O at 421, 520, and 598 cm^{-1} [21]. In the range of 4000-3500 cm^{-1}, three distinct bands at 3882.70, 3736.12, and 3610.74 cm^{-1} have been identified. These bands correspond to the O-H group, which is indicative of free alcohols such as hexane and iso-amyl alcohol. Furthermore, the well-defined peak at 677 cm^{-1} is attributed to the presence of iron-oxygen (Fe-O) bonds, confirming that the synthesized nanoparticles include iron oxide. Literature also reports the appearance of an Fe-O peak at approximately 631 cm^{-1}. Additionally, small peaks at 3873, 3726, and 3522 cm^{-1} are observed, which are due to the stretching of the hydroxyl O-H group. This group is commonly found in water molecules, which are often present on the surface of nanoparticles [27, 28].

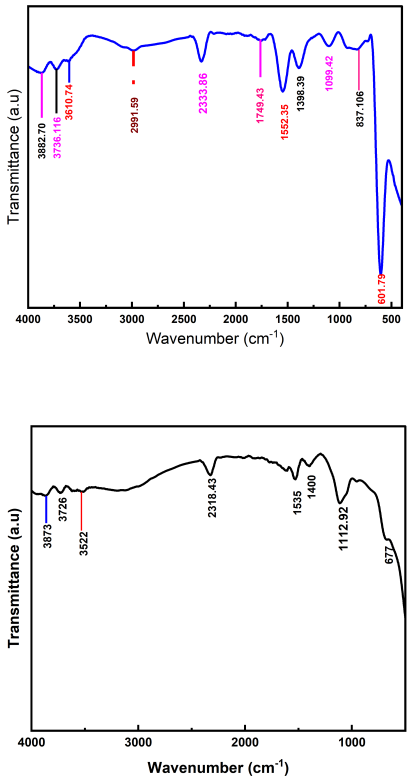

FIGURE 13: FT-IR spectrum of Copper (Cu) and Iron (Fe) nanoparticles synthesized through hexane oil phase.

FT-IR SPECTROSCOPY ANALYSIS OF CU@FE AND FE@CU BNP'S

Figure 14 and Figure 15 show the FT-IR analysis of Cu@Fe bimetallic nanoparticles synthesized with different concentrations of $NaBH_4$, specifically 0.15 grams and 0.35 grams. For the sample with 0.15 grams of $NaBH_4$, a peak at 601.79 cm^{-1} was observed, indicating the presence of Fe-O bonds. For the sample with 0.35 grams of $NaBH_4$, peaks at 439.77 cm^{-1} and 605.54 cm^{-1} were observed, corresponding to the stretching vibrations of Fe-O bonds in iron oxides. According to literature, Fe-O absorption bands are typically found at 465 cm^{-1}, 551 cm^{-1}, 455 cm^{-1}, 575 cm^{-1}, and 631 cm^{-1} [27].

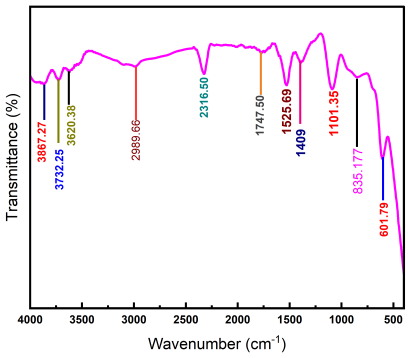

FIGURE 14: FT-IR spectrum of Cu@Fe BNP's with $NaBH_4$ 0.15 grams

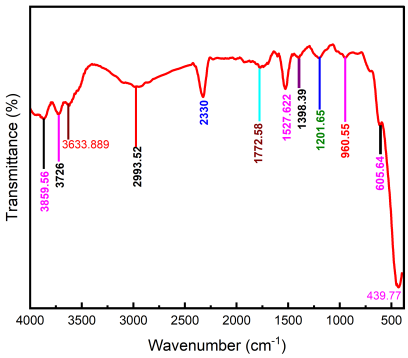

FIGURE 15: FT-IR spectrum of Cu@Fe BNP's with $NaBH_4$ 0.35 grams

Figure 16 and Figure 17 represent the FTIR analysis of Fe@Cu bimetallic nanoparticles synthesized with varying concentrations of $NaBH_4$, specifically 0.15 grams and 0.35 grams. In the sample with 0.15 grams of $NaBH_4$, a peak was observed at 680 cm^{-1}, indicating the presence of Cu-O bonds. In the sample with 0.35 grams of $NaBH_4$, a peak corresponding to the Cu-O bond was observed at

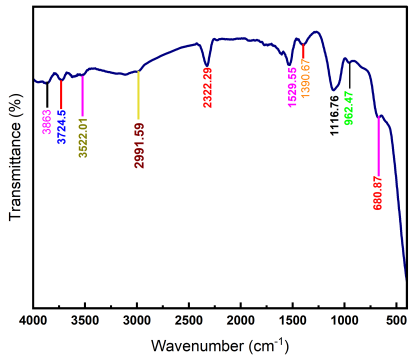

FIGURE 16: FT-IR spectrum of Fe@Cu BNP's with $NaBH_4$ 0.15 grams

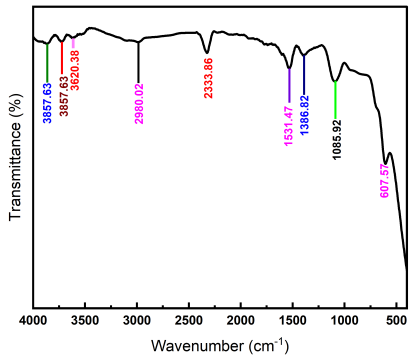

FIGURE 17: FT-IR spectrum of Fe@Cu BNP's with $NaBH_4$ 0.35 grams.

607.57 cm^{-1}, which falls within the literature range of (615-619) cm^{-1} [26].
The most prominent peaks are at 3863 cm^{-1} , 3724.50 cm^{-1} , 3522.01 cm^{-1} from Figure 16, and peaks at 3857.63 cm^{-1}, 3620.38 cm^{-1} from Figure 17 correspond to the stretching vibrations of the O-H bonds in water. The peak at 2991.59 cm^{-1} is due to the C-H asymmetric stretching. The peak at 2322.29 cm^{-1} corresponds to the stretching vibration of the C=O bond. The peaks at 1529.55 cm^{-1}, 1390.67 cm^{-1}, and 1116.70 cm^{-1} correspond to the stretching vibrations of the C=C, C-O, and C-OH bonds.

X-RD ANALYSIS OF FE@CU BNP'S

X-ray diffraction (XRD) patterns are a valuable tool for assessing the phase purity, crystallinity, and approximate size of crystallites in a sample. Figure 18 displays the XRD patterns of Fe@Cu bimetallic nanoparticles. The sample exhibits distinct XRD peaks at approximately 29.20°, 30.00°, 31.40°, 34.00°, 36.70°, 42.60°, 43.70°, 50.60°, 61.80°, 64.90°, and 74.10°(2θ).

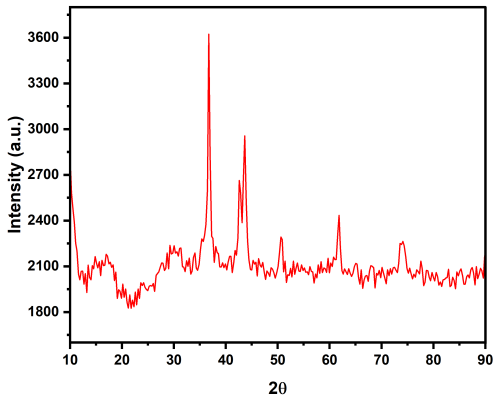

FIGURE 18: X-ray diffraction patterns of Fe@Cu bimetallic nanoparticles [29]

Specifically, the (2θ) values of 42.60°, 43.70°, 50.60°, and 74.10°correspond to the (1 1 1), (1 1 0), (2 0 0), and (2 2 0) peaks, respectively [30]. These peaks at (2θ) = 34.52°, 42.60°, 50.60°, and 74.10°are indicative of a face-centered cubic (fcc) structure, typically associated with copper [31–33]. However, it's worth noting that a smaller peak is observed at around 24.50°, 29.20°, 30.00°, 31.40°, 33.10°, 37.00°, and 61.80°, suggesting that a minor portion of copper has oxidized and transformed into copper oxide. In the literature, the peak at 61.80°is commonly attributed to the cuprite form of copper [34]. Furthermore, peaks at 65.10°and 83.00°indicate the presence of iron oxide. The emergence of a second prominent peak at 43.70°corresponds to the formation of iron particles. These values align with literature-reported values of 44.50°or 44.80°for iron peaks [35, 36].

Additionally, peaks at 35°and 65°are associated with copper oxide and iron oxide on the surface of the synthesized nanoparticles, respectively [37]. The presence of both Cu and Fe phases in the XRD patterns indicates that the Fe@Cu bimetallic nanoparticles are successfully formed. The size of the nanoparticles can be estimated using the Scherrer equation: $D = \frac{k\lambda}{\beta \cos\theta}$, where D is diameter of the particle, K is Scherrer constant (0.98), θ is diffraction angle, β is Full Width at Half Maximum (FWHM), λ (1.5406 Å) is the wavelength of X-ray [38].

TABLE I: Crystallite size of Fe@Cu BNP's using Scherrer equation

Angle Theta (θ)	(2θ)	FWHM (rad)	Size(D) nm	AVG. of D (nm)
36.74°	18.37°	0.51	17.24	
42.54°	21.27°	0.64	13.86	
43.46°	21.73°	1.24	7.21	14.52
50.70°	25.35°	0.54	17.12	
61.75°	30.87°	0.56	17.15	

Table I was used to calculate the average crystallite size of Fe@Cu BNP's, which was recorded as 14.52 nm, indicates that the BNP's do not possess perfect spherical symmetry. Instead, they exhibit a range of sizes, with an average diameter of 14.52 nm. Furthermore, it is observed that no additional particles are attached together in the sample.

To calculate the crystallite size of Fe@Cu BNP's, we employed the angle of diffraction (2θ) and utilized Origin software to determine the full width at half maximum (FWHM). FWHM is a critical parameter in X-ray diffraction (XRD) analysis with multiple applications, including phase identification, crystallite size determination, strain assessment, and the examination of microstructural features in materials.

TABLE II: Diffraction angles, d-spacing, and Miller indexes of Fe@Cu BNP's

λ (A°)	Angle (2θ)	Theta (θ)	d-spacing (A°)	index (hkl)
	36.74°	18.37°	2.44	(110)
	42.54°	21.27°	2.12	(111)
1.54	50.70°	25.35°	1.80	(200)
	61.75°	30.87°	1.52	(210)
	74.10°	37.05°	1.29	(220)

Table II shows the interplanar spacing (d-spacing) and Miller indices (hkl) for a cubic crystal. D-spacing is the distance between two adjacent planes of atoms in a crystal, and Miller indices are a set of three numbers that define the orientation of a plane of atoms in a crystal. Miller indices and d-spacing are essential components of Bragg's law, which explains how X-rays interact with crystals to produce diffraction patterns [39].

CONCLUSIONS

The research aimed to synthesize Fe@Cu nanoparticles using the microemulsion technique, a versatile method for producing nanoparticles with controlled size, morphology, and composition. UV-Vis spectroscopy of Fe@Cu BNP's showed a maximum peak at (312 $\pm$ 8.20) nm, with direct and indirect band gap energies of (2.54 $\pm$ 0.20, 0.26 $\pm$ 0.02) eV, where both the indirect and direct band gaps showed semiconductor behaviors. Furthermore, Fourier Transform Infrared spectroscopy of Fe@Cu bimetallic nanoparticles with peaks at 680.87 cm^{-1} and 607.57 cm^{-1} confirmed the presence of Cu-O bonds, consistent with Fe being in the core and Cu on the shell. The X-ray diffraction (XRD) patterns further reinforced the crystalline nature of the nanoparticles, with crystallite sizes falling within the range of 14.52 nm. The XRD graph also exhibited copper peaks at $(2\theta) = 34.52°$, 42.60°, 50.60°, and 74.10°, which are indicative of a face-centered cubic (fcc) structure. Additionally, the peak at 43.70°corresponded to the formation of iron particles. Notably, we also observed several oxide peaks for copper and iron particles at 24.50°, 29.20°, 30.00°, 31.40°, 33.10°, 37.00°, and 61.80°, suggesting that a minor portion of copper had oxidized and transformed into copper oxide. Peaks at 65.10°and 83.00°indicated the presence of iron oxide.

ACKNOWLEDGEMENTS

CONFLICT OF INTEREST

The authors declare that there is no conflict of interest regarding the publication of this paper.

REFERENCES

1. C. S. Brown, *Big history: From the big bang to the present*. The New Press, 2012.
2. A. Linde, D. Linde, and A. Mezhlumian, "From the big bang theory to the theory of a stationary universe," *Physical Review D*, vol. 49, no. 4, p. 1783, 1994.
3. A. Barhoum, M. L. García-Betancourt, J. Jeevanandam, E. A. Hussien, S. A. Mekkawy, M. Mostafa, M. M. Omran, M. S. Abdalla, and M. Bechelany, "Review on natural, incidental, bioinspired, and engineered nanomaterials: history, definitions, classifications, synthesis, properties, market, toxicities, risks, and regulations," *Nanomaterials*, vol. 12, no. 2, p. 177, 2022.
4. G. Sharma, A. Kumar, S. Sharma, M. Naushad, R. P. Dwivedi, Z. A. ALOthman, and G. T. Mola, "Novel development of nanoparticles to bimetallic nanoparticles and their composites: A review," *Journal of King Saud University-Science*, vol. 31, no. 2, pp. 257–269, 2019.
5. A. Mech, W. Wohlleben, A. Ghanem, V.-D. Hodoroaba, S. Weigel, F. Babick, R. Brüngel, C. M. Friedrich, K. Rasmussen, and H. Rauscher, "Nano or not nano? a structured approach for identifying nanomaterials according to the european commission's definition," *Small*, vol. 16, no. 36, p. 2002228, 2020.
6. P. Srinoi, Y.-T. Chen, V. Vittur, M. D. Marquez, and T. R. Lee, "Bimetallic nanoparticles: enhanced magnetic and optical properties for emerging biological applications," *Applied Sciences*, vol. 8, no. 7, p. 1106, 2018.
7. D. Schaming and H. Remita, "Nanotechnology: from the ancient time to nowadays," *Foundations of Chemistry*, vol. 17, pp. 187–205, 2015.
8. M. A. Malik, M. Y. Wani, and M. A. Hashim, "Microemulsion method: A novel route to synthesize organic and inorganic nanomaterials: 1st nano update," *Arabian journal of Chemistry*, vol. 5, no. 4, pp. 397–417, 2012.
9. B. K. Paul and S. P. Moulik, "Microemulsions: an overview," *Journal of Dispersion science and Technology*, vol. 18, no. 4, pp. 301–367, 1997.
10. R. N. Healy, R. L. Reed, and D. Stenmark, "Multiphase microemulsion systems," *Society of Petroleum Engineers Journal*, vol. 16, no. 03, pp. 147–160, 1976.
11. S. E. Friberg, C. Brancewicz, and D. S. Morrison, "O/w microemulsions and hydrotropes: the coupling action of a hydrotrope," *Langmuir*, vol. 10, no. 9, pp. 2945–2949, 1994.
12. I. Capek, "Preparation of metal nanoparticles in water-in-oil (w/o) microemulsions," *Advances in colloid and interface science*, vol. 110, no. 1-2, pp. 49–74, 2004.
13. J.-L. Salager, R. Marquez, M. Rondón, J. Bullón, and A. Graciaa, "Review on some confusion produced by the bicontinuous microemulsion terminology and its domains microcurvature: A simple spatiotemporal model at optimum formulation of surfactant-oil-water systems," *ACS omega*, vol. 8, no. 10, pp. 9040–9057, 2023.
14. U. Younas, S. Hassan, F. Ali, F. Hassan, Z. Saeed, M. Pervaiz, S. Khan, F. Jannat, S. Bibi, A. Sadiqa, *et al.*, "Radical scavenging and catalytic activity of fe-cu bimetallic nanoparticles synthesized from ixora finlaysoniana extract. coatings 2021, 11, 813," 2021.
15. Y. Abboud, T. Saffaj, A. Chagraoui, A. El Bouari, K. Brouzi, O. Tanane, and B. Ihssane, "Biosynthesis, characterization and antimicrobial activity of copper oxide nanoparticles (conps) produced using brown alga extract (bifurcaria bifurcata)," *Applied nanoscience*, vol. 4, pp. 571–576, 2014.
16. T. Klar, M. Perner, S. Grosse, G. Von Plessen, W. Spirkl, and J. Feldmann, "Surface-plasmon resonances in single metallic nanoparticles," *Physical Review Letters*, vol. 80, no. 19, p. 4249, 1998.
17. M. Aguilar, R. Esparza, and G. Rosas, "Synthesis of cu nanoparticles by chemical reduction method," *Transactions of Nonferrous Metals Society of China*, vol. 29, no. 7, pp. 1510–1515, 2019.
18. P. Makuła, M. Pacia, and W. Macyk, "How to correctly determine the band gap energy of modified semiconductor photocatalysts based on uv–vis spectra," 2018.
19. X. Li, H. Zhu, J. Wei, K. Wang, E. Xu, Z. Li, and D. Wu, "Determination of band gaps of self-assembled carbon nanotube films using tauc/davis–mott model," *Applied Physics A*, vol. 97, pp. 341–344, 2009.
20. J. Tauc, "Optical properties of solids, edited by s. nudelman and ss mitra," 1969.
21. M. Vaseem, A. Umar, S. H. Kim, and Y.-B. Hahn, "Low-temperature synthesis of flower-shaped cuo nanostructures by solution process: formation mechanism and structural properties," *The Journal of Physical Chemistry C*, vol. 112, no. 15, pp. 5729–5735, 2008.
22. H. Zhang, X. Zhang, H. Li, Z. Qu, S. Fan, and M. Ji, "Hierarchical growth of cu2o double tower-tip-like nanostructures in water/oil microemulsion," *Crystal growth & design*, vol. 7, no. 4, pp. 820–824, 2007.

23. A. J. Deotale and R. Nandedkar, "Correlation between particle size, strain and band gap of iron oxide nanoparticles," *Materials Today: Proceedings*, vol. 3, no. 6, pp. 2069–2076, 2016.
24. A. Visibile, R. B. Wang, A. Vertova, S. Rondinini, A. Minguzzi, E. Ahlberg, and M. Busch, "Influence of strain on the band gap of cu2o," *Chemistry of Materials*, vol. 31, no. 13, pp. 4787–4792, 2019.
25. M. Dongol, M. El-Nahass, A. El-Denglawey, A. Elhady, and A. Abuelwafa, "Optical properties of nano 5, 10, 15, 20-tetraphenyl-21h, 23h-prophyrin nickel (ii) thin films," *Current Applied Physics*, vol. 12, no. 4, pp. 1178–1184, 2012.
26. N. Ullah, A. Ullah, and S. Rasheed, "Green synthesis of copper nanoparticles using extract of dicliptera roxburghiana, their characterization and photocatalytic activity against methylene blue degradation," *Lett. Appl. NanoBioSci*, vol. 9, pp. 897–901, 2020.
27. S. Hwang, A. Umar, G. Dar, S. Kim, and R. Badran, "Synthesis and characterization of iron oxide nanoparticles for phenyl hydrazine sensor applications," *Sensor Letters*, vol. 12, no. 1, pp. 97–101, 2014.
28. X. Liu, "Ir spectrum and characteristic absorption bands," *Organic Chemistry I; Kwantlen Polytechnic University: Surrey, BC, Canada*, 2021.
29. N. G. Dlamini, A. K. Basson, and V. S. R. Pullabhotla, "Synthesis and application of fecu bimetallic nanoparticles in coal mine wastewater treatment," *Minerals*, vol. 11, no. 2, p. 132, 2021.
30. M. Raja, J. Subha, F. B. Ali, and S. H. Ryu, "Synthesis of copper nanoparticles by electroreduction process," *Materials and Manufacturing Processes*, vol. 23, no. 8, pp. 782–785, 2008.
31. A. T. Joseph, P. Prakash, and S. Narvi, "Phytofabrication and characterization of copper nanoparticles using allium sativum and its antibacterial activity," *Int. J. Sci. Eng. Technol*, vol. 4, pp. 463–472, 2016.
32. T. Shubair, O. Eljamal, A. M. Khalil, A. Tahara, and N. Matsunaga, "Novel application of nanoscale zero valent iron and bimetallic nano-fe/cu particles for the treatment of cesium contaminated water," *Journal of environmental chemical engineering*, vol. 6, no. 4, pp. 4253–4264, 2018.
33. J. Ramyadevi, K. Jeyasubramanian, A. Marikani, G. Rajakumar, A. A. Rahuman, T. Santhoshkumar, A. V. Kirthi, C. Jayaseelan, and S. Marimuthu, "Copper nanoparticles synthesized by polyol process used to control hematophagous parasites," *Parasitology research*, vol. 109, pp. 1403–1415, 2011.
34. P. Sepúlveda, M. A. Rubio, S. E. Baltazar, J. Rojas-Nunez, J. S. Llamazares, A. G. Garcia, and N. Arancibia-Miranda, "As (v) removal capacity of fecu bimetallic nanoparticles in aqueous solutions: the influence of cu content and morphologic changes in bimetallic nanoparticles," *Journal of colloid and interface science*, vol. 524, pp. 177–187, 2018.
35. A. Tavasoli, M. Trépanier, R. M. M. Abbaslou, A. K. Dalai, and N. Abatzoglou, "Fischer–tropsch synthesis on mono-and bimetallic co and fe catalysts supported on carbon nanotubes," *Fuel Processing Technology*, vol. 90, no. 12, pp. 1486–1494, 2009.
36. Q. Wang, S. R. Kanel, H. Park, A. Ryu, and H. Choi, "Controllable synthesis, characterization, and magnetic properties of nanoscale zerovalent iron with specific high brunauer–emmett–teller surface area," *Journal of Nanoparticle Research*, vol. 11, pp. 749–755, 2009.
37. K. Ulucan-Altuntas, A. E. Hadki, L. Bilgili, A. Y. Çetinkaya, S. L. Kuzu, and E. Debik, "Iron–copper bimetallic nanoparticle for the removal of disinfection by-products: Optimization, kinetic study, and life cycle assessment," *Water, Air, & Soil Pollution*, vol. 233, no. 7, p. 272, 2022.
38. M. A. Thakar, S. S. Jha, K. Phasinam, R. Manne, Y. Qureshi, and V. H. Babu, "X ray diffraction (xrd) analysis and evaluation of antioxidant activity of copper oxide nanoparticles synthesized from leaf extract of cissus vitiginea," *Materials Today: Proceedings*, vol. 51, pp. 319–324, 2022.
39. T. Theivasanthi and M. Alagar, "Titanium dioxide (tio2) nanoparticles xrd analyses: an insight," *arXiv preprint arXiv:1307.1091*, 2013.